Front. Optoelectron. 2012, 5(1): 21–40
DOI 10.1007/s12200-012-0192-y

REVIEW ARTICLE

Designs and experiments on infrared two-dimensional silicon photonic crystal slab devices

Lin GAN, Zhiyuan LI (✉)

Laboratory of Optical Physics, Institute of Physics, Chinese Academy of Sciences, Beijing 100190, China

Abstract Photonic crystal (PhC) has offered a powerful means to mold the flow of light and manipulate light-matter interaction at subwavelength scale. Silicon has a large refraction index and low loss in infrared wavelengths, which makes it an important optical material. And silicon has been widely used for integrated photonics applications. In this paper, we have reviewed some recent theoretical and experimental works in our group on infrared two-dimensional (2D) air-bridged silicon PhC slab devices that are based on both band gap and band structure engineering. We have designed, fabricated, and characterized a series of PhC waveguides with novel geometries, PhC high-quality (high-Q) cavity, and channel drop filters utilizing resonant coupling between waveguide and cavity. These devices are aimed to construct a more flexible network of transport channel for infrared light at micrometer/nanometer scale. We have also explored the remarkable dispersion properties of PhCs by engineering the band structures to achieve negative refraction, self-collimation, superprism, and other anomalous dispersion behaviors of infrared light beam. Furthermore, we have designed and fabricated a PhC structure with negative refraction effect and used scanning near-field optical microscopy to observe the negative refraction beam. Finally, we have designed and realized a PhC structure that exhibits a self-collimation effect in a wide angle range and with a large bandwidth. Our works presented in this review show that PhCs have a strong power of controlling propagation of light at micrometer/nanometer scale and possess a great potential of applications in integrated photonic circuits.

Keywords photonic crystal (PhC), waveguide, high-quality (high-Q) cavity, channel-drop filter, negative refraction

1 Introduction

During the past two decades, there have been great interests in developing ways to manipulate photons at nanoscale, realizing optical integrations, developing smaller, faster, and more efficient optoelectronic devices for the purpose of next-generation optoelectronic technology. Great progresses have been made in exploring photonic crystals (PhCs) [1,2], plasmonic structures [3,4], and other nanophotonic devices for applications. However, plasmonic structures always involve some metal cells and are subject to strong energy dissipation and absorption loss in optical frequencies. Since silicon has a large refraction index and low loss in the infrared wavelength, it becomes an important optical material that has been widely used for integrated photonics applications. Meanwhile, silicon dominates microelectronics and this makes the silicon-based optical devices have the advantage to integrate with electronic devices.

Among all the semiconductor-based optical devices, a class of integrated optical devices that are built in the platform of periodically patterned silicon structures (namely, silicon PhCs) are now attracting much attention [5–7]. Analogous to real crystal, electromagnetic (EM) wave is strongly modulated in PhC by means of periodic Bragg scattering. Photonic band gaps (PBGs), which can prevent light from propagation in certain direction for a certain range of wavelengths, are formed similarly to electron band gaps. If we introduce a line defect or a point defect in PhC, a defect state will take place within the PBG, where light is strongly localized around the defect. These defects can serve as a high efficient waveguide channel or as a micro-cavity with a high-quality (high-Q) factor. In addition, the transmission bands also provide remarkable dispersion properties due to strong Bragg scattering, and negative refraction, self-collimation, superprism and many other anomalous transport behaviors [8–13] can be achieved by engineering the unit cell geometry of PhCs. In this review, we briefly introduce the theoretical

Received September 13, 2011; accepted November 8, 2011

E-mail: lizy@aphy.iphy.ac.cn

background of the light propagation in PhC and show our recent results on design, fabrication, and characterization of several basic integrated optical devices in the platform of infrared silicon PhC slab.

2 Theoretical and numerical tools

In this section, we briefly introduce the theoretical background and the numerical methods for our study of PhC. The propagation of EM waves in PhC is governed by the Maxwell equations [14]. For the sake of simplicity, here we consider a nonmagnetic linear system. In particular, the dielectric constant ε is independent of frequency and we neglect any absorption of EM waves by the material. Furthermore, there are no free charges or currents in our system. With all of the assumptions, the magnetic field within the PhC satisfies the following equation that directly originates from the Maxwell equations [15]:

$$\nabla \times \left\{ \frac{1}{\varepsilon(\boldsymbol{r})} \nabla \times \boldsymbol{H}(\boldsymbol{r}) \right\} = \frac{\omega^2}{c^2} \boldsymbol{H}(\boldsymbol{r}). \tag{1}$$

Since our system involves a periodic dielectric function ε, we can apply Bloch-Floquet theorem to our situation, which means that the solutions can be expressed as:

$$\boldsymbol{H}_{\boldsymbol{k}}(\boldsymbol{r}) = \boldsymbol{u}_{\boldsymbol{k}}(\boldsymbol{r}) \mathrm{e}^{\mathrm{i}(\boldsymbol{k}\cdot\boldsymbol{r} - \omega t)}, \tag{2}$$

where $\boldsymbol{k}$ is the Bloch wave vector and $\boldsymbol{u}_{\boldsymbol{k}}(\boldsymbol{r})$ is a periodic function of position. This type of solutions are periodic as a function of $\boldsymbol{k}$.

Several theoretical methods have been developed to handle different problems for PhC structures, such as the plane-wave expansion method (PWEM) [15–18], transfer matrix method (TMM) [19], finite-difference time-domain (FDTD) method [20,21], and multiple scattering method [22,23]. Each method exhibits its own benefits and drawbacks. The PWEM is the earliest method applied to PhC [15]. It has shown its great power in the discovery of three-dimensional (3D) diamond-lattice PhCs that have a complete PBG [15]. However, this method has a severe limitation in that it can only deal with the photonic band structures. The TMM is an efficient approach that was designed particularly to calculate the transmission spectra of PhC, but it can also be used to solve the photonic band structures. This approach works based on the finite-difference scheme in the real space [19]. Later on, a plane-wave based transfer-matrix method (PWTMM) was developed by Li et al. [24–26]. This method works on the plane-wave space and uses plane wave functions (representing Bragg waves) to describe both the EM fields and dielectric functions. This approach can handle a broad range of general PhC problems. In addition to the regular solutions of photonic band structures and transmission/reflection/absorption spectra, this approach can efficiently solve the Bloch wave scattering at the interface between semi-infinite PhC structures, because it can also work in the Bloch mode space [27]. So far, other methods have not been developed such a peculiar capability. For this reason, it can be used to calculate efficiently modal coupling with multimode PhC waveguides [28], transmission efficiency through general two-dimensional (2D) and 3D waveguide bends [29], and band diagrams and field profiles of PhC surface states [30]. On the other hand, this method has adopted advanced numerical and mathematical analysis tools to enhance numerical convergence and accuracy, and it has shown its superior power in dealing with some metal PhC structures compared with other methods [31]. Recently, this method has been also extended to solve nonlinear optical problems in ferroelectric PhC structures [32,33].

FDTD method is a very popular and universal approach in numerical simulations of various PhC problems. In addition to the regular band structures and optical spectra calculations, this technique can govern the EM field evolution with time in arbitrary PhC structures with infinite or finite structural domain. The reason is that the technique works in the time domain and directly solves the Maxwell equations.

Many free software packages and commercial software packages have been developed worldwide and they are widely used in numerical simulations and solutions of different PhC problems. Our group has also developed homemade codes based on several methods including the PWEM, PWTMM, FDTD, and multiple scattering method. In addition, we also utilize publicly available free software packages as they are more numerically economic or have better numerical efficiency. In our case, we use MIT Photonic-Bands (MPB) package [16] to compute the photonic band structures and use MEEP, a free FDTD simulation software package developed at MIT [34] to calculate transmission spectra and model EM wave transport features in the 2D PhC structures and devices.

3 Sample fabrication and optical characterization

After the discovery of PhC, many novel devices have been proposed to control light and implement specific functionality of information processing. 2D air-bridged silicon PhC slab (Fig. 1(a)) is an excellent platform to fabricate PhC integrated optical devices. This system involves a silicon membrane suspended in air, which confines light by high index contrast in the vertical direction, while the periodic structures in the slab give a strong in-plane confinement of light through PBGs. In most cases, a typical PhC structure is a kind of periodic array of air holes etching in a silicon-on-insulator (SOI) wafer by microfabrication techniques. The SOI wafer has a Si/SiO_2/Si structure. In our case, it has a 220 nm thick silicon top layer and a 3 μm buried silica

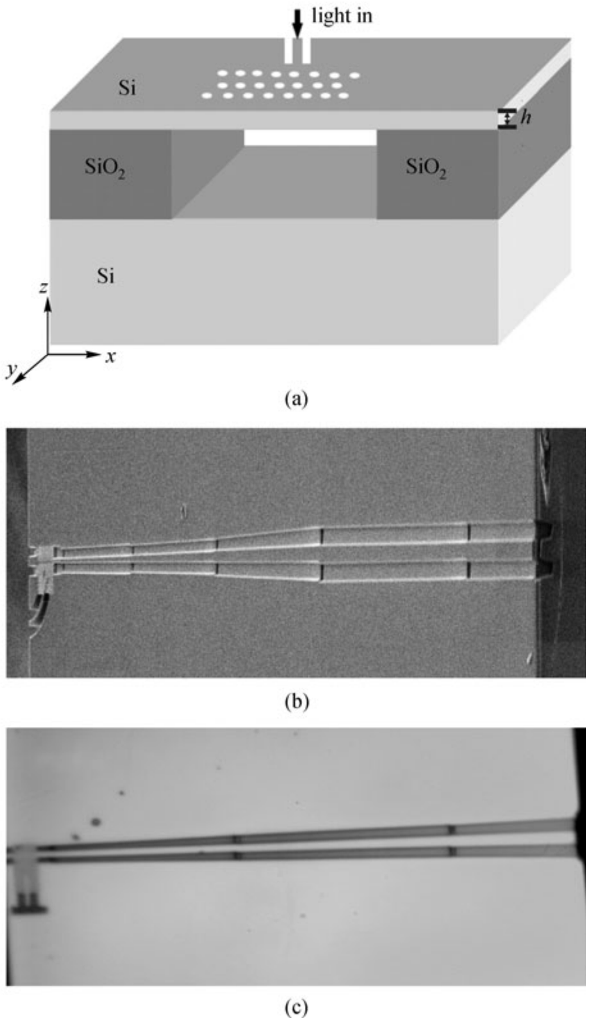

Fig. 1 (a) Schematic view of 2D air-bridged PhC structures with input silicon waveguide. Whole structures are fabricated in SOI wafer. Air-bridged structures are formed by HF wet etching; (b) and (c) are top-view SEM and optical microscopy image of practical PhC sample used in experiment. Long adiabatically tapering ridge waveguide connected with PhC structure can be clearly visualized

layer on top of a 0.5 mm thick single crystal silicon wafer. We directly use focused ion beam (FIB) lithography to drill air holes in the silicon membrane or use electron-beam lithography (EBL) to define PhC patterns in a thin film of polymethylmethacrylate (PMMA), and then transfer the patterns into the silicon membrane by inductively coupled plasma (ICP) etching under the atmosphere of SF$_6$ and C$_4$F$_8$ gases. Figures 1(b) and (c) are the top-view scanning electron microscope (SEM) picture of our PhC structures fabricated by FIB. By utilizing state-of-the-art microfabrication techniques, the optical properties of the periodic array of air holes can be easily and accurately controlled. For instance, one can change the diameters of certain holes or omit to etch one or several holes at certain places. These procedures can allow for engineering of the linear and point defect characteristics. After the air holes PhC structures get done, we use HF acid wet etching to remove the buried oxide layer under the silicon membrane PhC structures to form air-bridged structures. Usually, wide silicon wire waveguides (also with the air-bridged geometry) close to the interface of PhC structures are used as the input and output infrared light beam channels, as shown in Fig. 1. These wire waveguides are further connected with long adiabatically tapering ridge silicon waveguides (each about 0.2 mm long) to allow easy coupling with external infrared signals. As a result, a typical PhC sample has a total length of about 0.5 mm and the input and output ends are carefully polished to enhance the coupling efficiency of input and output infrared signals.

The transmission spectra of a PhC structure effectively reflect its optical properties. To get this important physical quantity, we have set up an experimental apparatus that involves several functional components. The overall measurement setup is schematically illustrated in Fig. 2(a), while a picture of the corresponding real system is displayed in Fig. 2(b). As shown in Fig. 2(a), the PhC samples are placed in the center of the stage, with its two sides connected with the input and output optical fibers. The input optical signal comes from a continuous wave tunable semiconductor laser with the wavelength ranging from 1500 to 1640 nm, launched into one facet of the ridge waveguide via a single-mode lensed fiber. Power meter is used to detect the optical signals transmitted through the PhC structures and emitted from the output side. The measurement is made with transverse magnetic (TE) polarization (electric field parallel to the slab plane) since it has a complete band gap in silicon PhC slabs. The measurement data are normalized by a ridge waveguide on silicon with the same length and width to yield the final transmission spectra for a specific PhC structure.

In addition to the measurement of transmission spectra, our experimental setup can offer another big power: it allows for easy and convenient direct monitoring of the transport path of infrared light through PhC devices. As depicted in Fig. 2(a), a CCD camera is mounted above the sample and it can *in situ* monitors the transport property by imaging the roughness induced scattering infrared light from the surface of the PhC structures. The long-focus microscope objective connected with the CCD camera is shown in the upper part of Fig. 2(b). The ray trace can be directly visualized by the camera to yield images at a personal computer monitor, and this gives the researcher a rough but direct estimate about how much the infrared signal has gone into the PhC structures. The idea is simple: if the infrared light is coupled into the PhC sample with a sufficiently high efficiency, infrared light can transport along the input ridge waveguide, PhC devices, and the output ridge waveguide. Significant scattering of infrared signal off the sample can take place and is collected by the CCD camera and visualized *in situ* by the monitor. The strongest scattering occurs at the discontinuity interface, including the end facets of input and output ridge

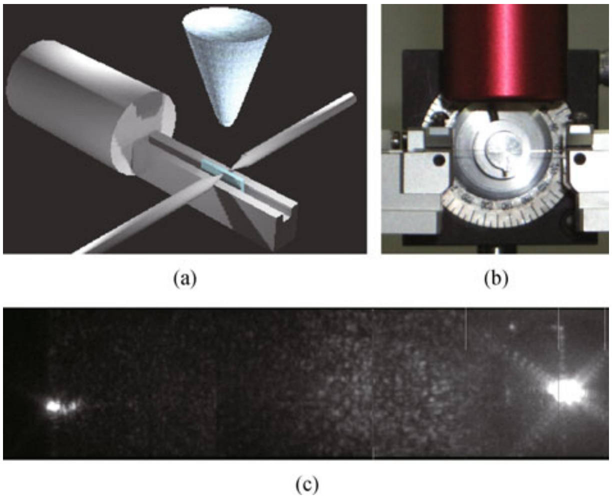

Fig. 2 (a) Schematic view and (b) experimental setup for optical characterization of infrared 2D silicon PhC slab structures; (c) typical optical microscopy picture recorded by CCD camera for PhC sample as displayed in Fig. 1(b)

waveguides and the connection section between ridge waveguides and PhC structures. Even within the PhC structures, remarkable scattering still takes place because of the inevitable roughness on the surface of silicon slab and within the inner walls of air holes. On the other hand, if the infrared signal coupled into the PhC samples is weak, then the overall scattering light that can be collected by the CCD camera is also very weak, and no picture can be visualized in the monitor. Figure 2(c) shows a typical microscopy picture recorded by the CCD camera. Such an experimental setup is very convenient to adjust the precise position of the input and output optical fibers, so that they have a precise point-to-point alignment with about 250 nm thick PhC samples to allow for high-efficiency optical coupling. The infrared signal transporting through the PhC samples usually has a power level of micro-walt when the input signal from semiconductor laser is on the power level of milli-walt. The signal has been already sufficiently strong to allow for transmission spectrum measurement and CCD camera monitoring with high signal-to-noise ratio.

4 PhC band-gap devices: waveguides and cavities

4.1 PhC waveguides

PhC waveguides are one of the most important elements in PhC integrated optics, because they offer efficient channels for light propagating at wavelength scale and connect different devices in integrated optical circuits. Usually, PhC waveguides are formed by removing one row of holes in a PhC structure. The line defects can generate defect states within the complete PBG and serve as waveguide channels for light to propagate efficiently and freely in PhC structures. Among many 2D PhC slab structures, the triangular lattice of air holes has a relatively large band gap for TE-like EM modes, where the magnetic field points in the perpendicular direction while the electric field is dominantly within the lateral plane of the slab. In addition, the structures allow for easy fabrication by standard planar nanofabrication technologies such as FIB and EBL, and have good mechanical stability. For these reasons, they are widely and dominantly adopted in designing and exploring PhC based integrated optical devices [35,36].

Figure 3(a) shows the calculated TE-like mode photonic band structures of a particular 2D triangular lattice PhC slab, where a wide complete PBG is clearly seen. In the region, light propagation inside the PhC is prohibited. When removing one or several rows of air holes in the PhC structures, some allowed modes (defect states) appear within the PBG (Fig. 3(b)), and they can be used to create waveguides or cavities. In most works, single-mode or multi-mode optical waveguides are usually made along the $\Gamma-\mathrm{K}$ direction in the triangular lattice PhC. It has been well established in plenty of literatures that the number of waveguide modes as well as the width of the transmission windows can be controlled by tuning the core width of the line defects. However, waveguides along other directions in the triangular lattice PhC were rarely discussed. Just like the $\Gamma-\mathrm{K}$ direction, waveguides along the $\Gamma-\mathrm{M}$ direction should also be able to guide confined modes due to the existence of a complete PBG in the 2D triangular lattice PhC. By removing a line of diamond areas, we can obtain a cluster-like waveguide along the $\Gamma-\mathrm{M}$ direction as depicted in Fig. 4(a). This kind of waveguide is called $\Gamma-\mathrm{M}$ waveguide [37].

Figure 4(b) is the SEM picture of the original $\Gamma-\mathrm{M}$ waveguide, where the air holes remain to locate at the original lattice site and the radius of all air holes remains the same. The air holes are directly drilled by FIB and the lattice constant is 430 nm. According to our simulation and experiment results, we find that the width of the propagation modes for the original $\Gamma-\mathrm{M}$ waveguide (Fig. 4(b)) is only 22 nm. Then we optimize the geometry to improve its transmission characteristics. We shrink the radius r_1 of the air holes in the two nearest-neighboring rows around the waveguide and enlarge the radius r_2 of the air holes in the two second-nearest-neighboring rows, as shown in Fig. 4(c). The key point is to generate a transport pathway with walls as smooth as possible. According to our simulations, the parameters corresponding to an optimized waveguide are that $r_1 = 50\,\mathrm{nm}$ and $r_2 = 170\,\mathrm{nm}$, while the radius of the original air holes is $r_0 = 120\,\mathrm{nm}$. Figures 5(a) and (b) are the calculated dispersion relations of the original and optimized $\Gamma-\mathrm{M}$ waveguide, respectively. It's shown that the optimized waveguides have a high pass band that is much broader than the original waveguide. We can also obtain the same

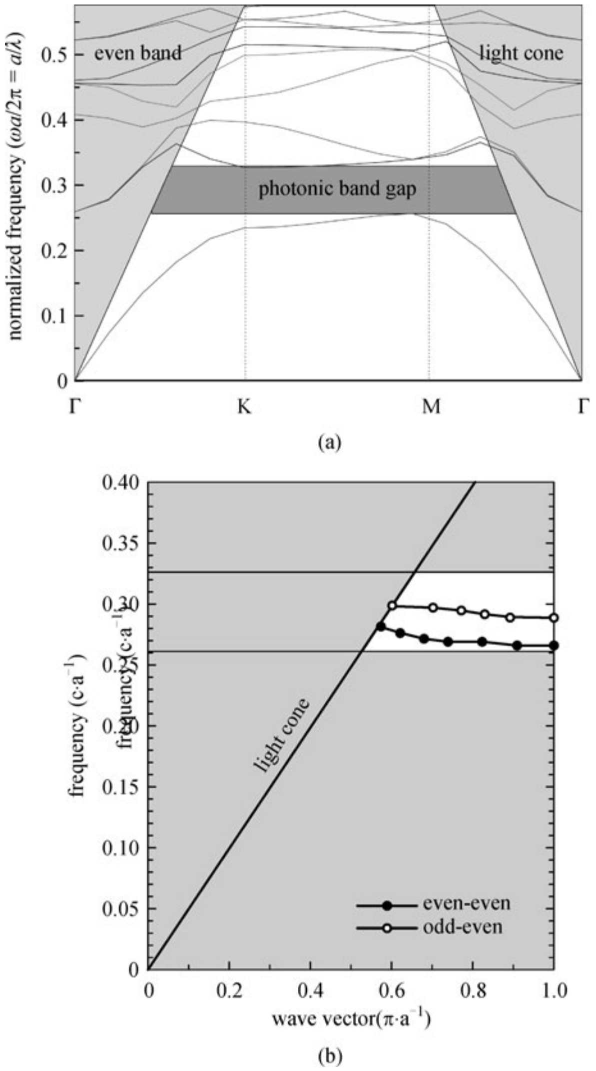

(a)

(b)

Fig. 3 (a) Photonic band structures for air holes triangular lattice PhC slab; (b) band diagrams for PhC W1 waveguide. The upper and lower bands correspond to even-symmetric and odd-symmetric guided mode, respectively

conclusion from the measured transmission spectra in Figs. 5(c) and 5(d). Besides, the intensities of the transmission spectra are much higher than the original one. As the Γ – M waveguide is perpendicular to the usual Γ – K waveguide, it offers an alternative to construct a waveguide interconnection beyond the usual scheme of Γ – K with Γ – K waveguides. A high-performance wide-band Γ – M waveguide should be of great help to build integrated-optical devices, such as interconnection networks, channel-drop filters, and wave division multiplexers, with more flexible geometrical configurations in 2D PhC slabs.

Based on the design of an optimized Γ – M waveguide, we combine the Γ – K waveguide and Γ – M waveguide together to form a 90° waveguide bend as schematically depicted in Fig. 6(a) [38]. This is the first design of a 90° waveguide bend in the 2D triangular-lattice PhC. The whole waveguide bend system is composed of two Γ – K waveguides as the input and output ports and the center Γ – M waveguide as the connection component. In other words, the structure involves two consecutive segments of 90° waveguide bends.

In constructing the waveguide bend, we have used the optimized Γ – M waveguide discussed in the above and depicted in Fig. 4(c). The guided modes in the optimized Γ – M waveguide have better phase-matching and mode profile matching with the normal Γ – K waveguides. In the same time, we modify the bend corner geometry by fabricating smaller air holes in the corner to make the guided modes between the two kinds of waveguides matching better. Based on a serial of simulation and experiment tests, we find the best values for r_1 and r_2. Figure 6(b) shows the SEM picture of the waveguide bend with r_1 = 50 nm and r_2 = 150 nm. After optimization, we get 70 nm pass band width while the transmission efficiency of a single bend is 45%. The proposed 90° waveguide bends can help to construct integrated optical circuits with more flexible and diversified infrastructures.

4.2 Coupled-cavity waveguide

Moreover, we have designed an air-bridged silicon-based photonic crystal coupled-cavity waveguides (PCCCWs) [39] and mapped its near-field optical distributions at different wavelengths around 1550 nm with the scanning near-field optical microscopy (SNOM) technology. For PCCCWs, the eigenmodes usually have relatively narrow bandwidth with slow group velocity in the whole band range. Till now, slow light propagation in such specific PCCCWs is still not experimentally studied via SNOM technique. Figures 7(b)–7(f) show the calculated optical field distribution profiles at different wavelengths with a simulation model schematized in Fig. 7(a). We fabricated the PCCCW in the SOI wafers with FIB system. Figure 8(a) displays the SEM image of the element composed of the central PCCCW (encircled by a red square), two identical W1 PhC waveguides, and the input/output ridge waveguides. Figure 8(b)–8(f) displays the near-field optical intensity distribution patterns of the PCCCW at different wavelengths. The scanning area is 12 μm × 15 μm with the incident light propagating upwards from the bottom of the image. Straight yellow lines in Figs. 8(b)–8(f) are used to label the position for showing the cross-sectional profiles of the field distribution patterns.

The optical intensity distribution patterns are different at 1550 and 1610 nm, even though both of them mainly appear as a single narrow line along the central PCCCW region with a full width at half maximum (FWHM) of about 350 nm. Precisely speaking, the pattern demonstrates a little bit shoulder as a result of mode superposition at 1550 nm, since it comprises two eigenmodes. At 1610 nm, the calculated result consists well with the experimental

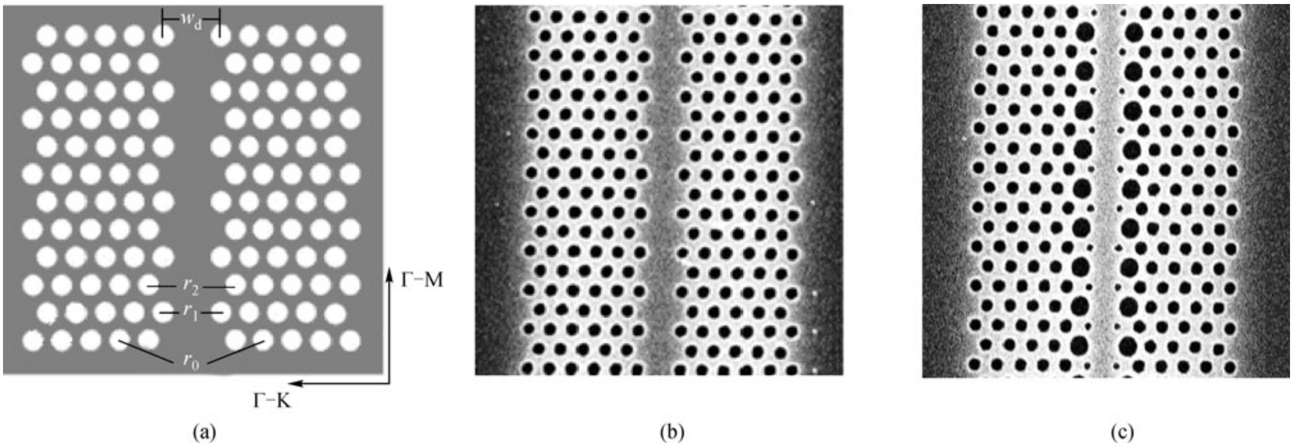

Fig. 4 (a) Schematic of Γ–M waveguide constructed in a triangular-lattice PhC slab. The width of the waveguide w_d, as well as the radius of air holes in the first and second row r_1 and r_2, are the three crucial parameters to optimize the width of the transmission windows; (b) and (c) are SEM pictures of original and optimized Γ–M waveguides

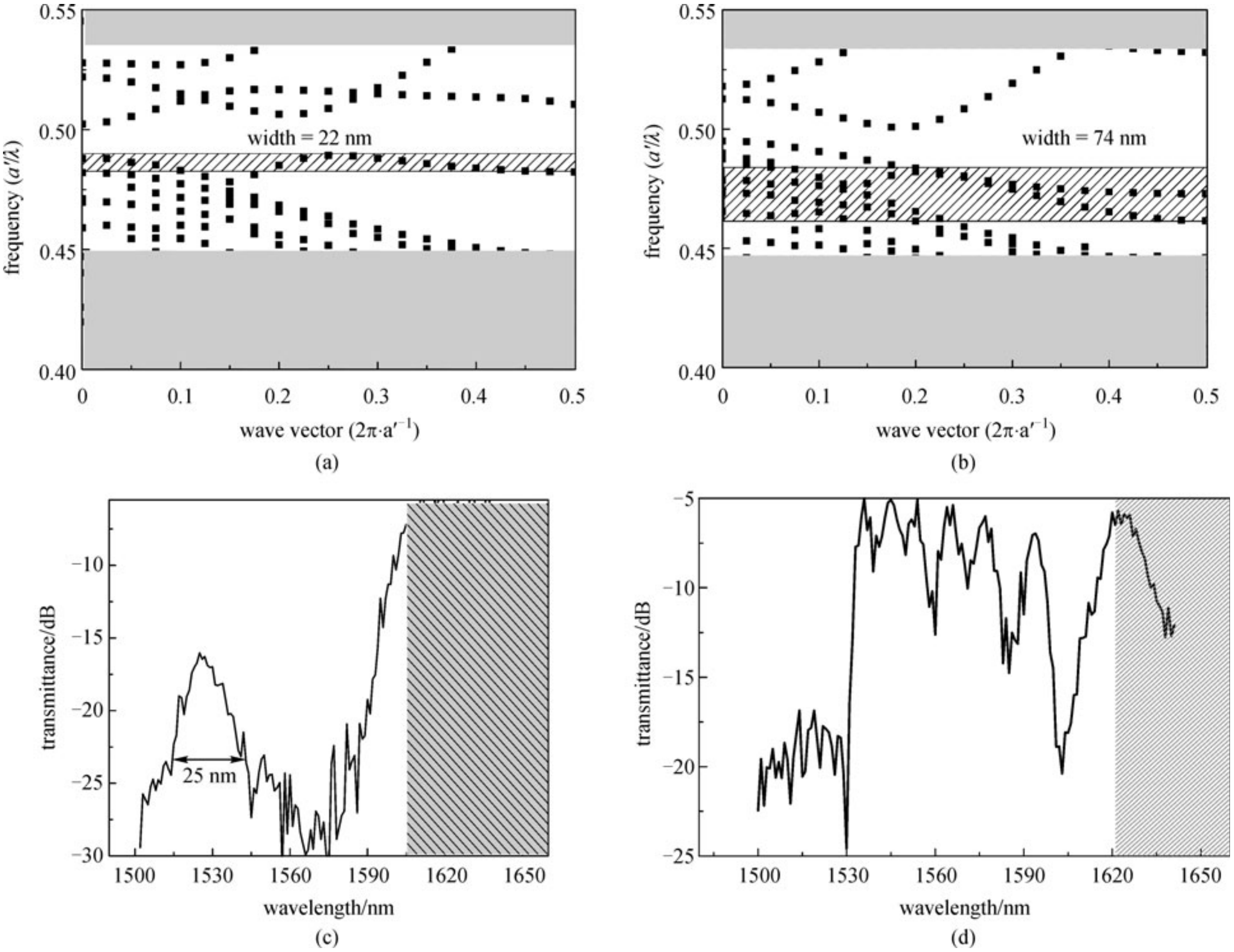

Fig. 5 Calculated modal dispersion relation of (a) original Γ–M waveguide and (b) optimized Γ–M waveguide. The band width of the waveguide modes (within the dashed boxes) is 22 nm in the original waveguide, which has parameters: lattice constant $a = 430$ nm, hole radius $r_0 = r_1 = r_2 = 120$ nm, and waveguide width $w_0 = 2a$. After optimization by the following parameters as $a = 430$ nm, $r_1 = 50$ nm, $r_2 = 170$ nm, and $w_d = 0.65w_0$, the waveguide band width is significantly broadened to 74 nm; (c) and (d) are the corresponding measured transmission spectra of the original and optimized waveguides

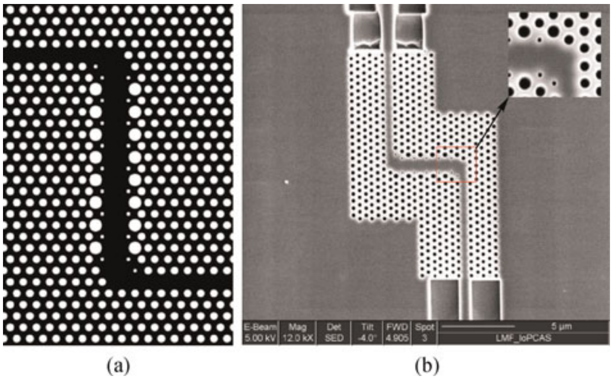

Fig. 6 (a) Schematic geometry of 90° waveguide bends in a triangular lattice PhC slab with optimized Γ–M waveguide; (b) SEM picture of practical sample of 90° waveguide bends with optimized bend corner geometry

one in Fig. 8(f) presented a single line along the whole waveguide. The pattern appears bright and wide with obvious interference nodes in the PCCCW section. The simulated field distribution profiles in the W1 PhC waveguide sections agree well with the detected ones at all these wavelengths, which show a snake-like/single-line profile in the input/output W1 PhC waveguide except that of a snake-like profile in the output W1 PhC waveguide at 1560 nm. In addition, the simulated field distribution patterns of the snake-like profile in the PCCCW section appear deviating greatly from the detected ones at 1550, 1571, and 1590 nm. However, if we calculate the optical field distribution patterns at 1550, 1560, and 1571 nm with the even-to-odd amplitude ratios of 1∶4, 1∶1, 1∶4, and 1∶6, respectively, we can find the simulated results are consistent with the experimental patterns evolving from single, to snake-like, and then to double-line structures for the PCCCW section. Combination of the near-field optical detection and theoretical simulation shows that SNOM is an efficient tool to study the optical propagation in the PCCCW and can help to design slow light elements.

4.3 High-*Q* cavity

Quantum information processing and quantum state manipulation have received great attentions because of their potential revolutionary impact on our future network communication. Optical cavities, which can be used to

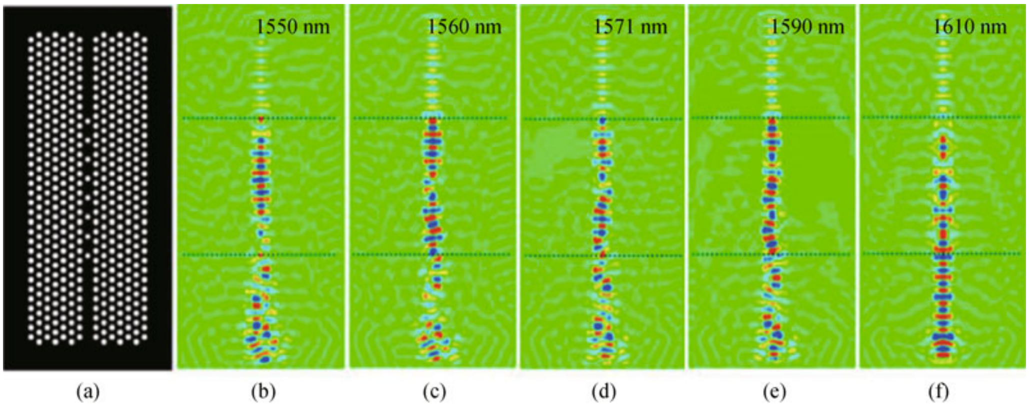

Fig. 7 Simulation model (a) and calculated optical field distributions at (b) 1550 nm; (c) 1560 nm; (d) 1571 nm; (e) 1590 nm and (f) 1610 nm

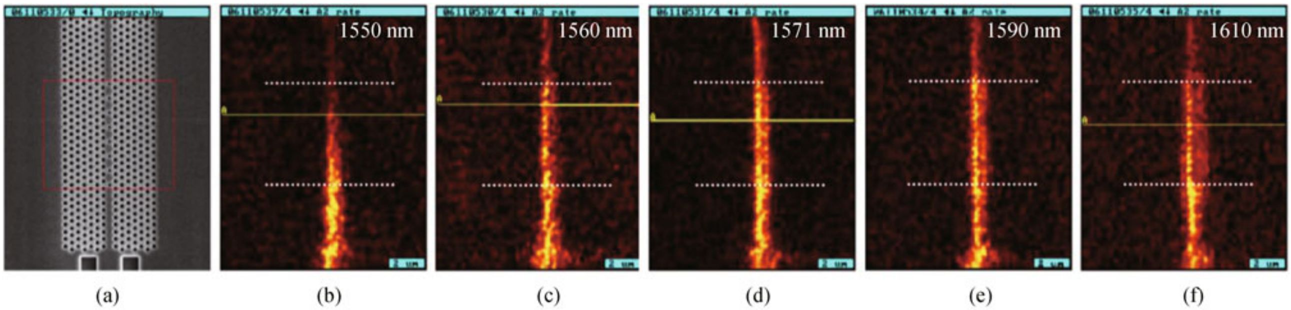

Fig. 8 (a) SEM topographic image, and near-field optical intensity distributions at (b) 1550 nm; (c) 1560 nm; (d) 1571 nm; (e) 1590 nm and (f) 1610 nm. White dotted lines in each optical picture denote the interface between W1 PhC waveguide and PCCCW. All pictures were obtained for the same scanning area of 12 μm × 15 μm

store information, are considered to be one of the most important devices in the quantum communication application. The generation and teleportation of qubits require sufficiently high value of Q/V, where V stands for the mode volume of the optical cavities. As a result, high-Q optical cavities show great potential application in quantum information. Among all the optical cavities, 2D PhC slab cavities are the best choice for their high-Q and small mode volume characteristics. It has been reported that Rabi splitting can be observed experimentally when the quantum dots are introduced into the PhC cavities with high Q/V [40,41]. Moreover, due to the development of nanofabrication technique, multiple high-Q PhC slab cavities can be fabricated at the same time on a single slab by the EBL and ICP etching technique. Once embedding atoms or quantum dots into the high-Q PhC cavities, various quantum phenomena can be demonstrated on chip. Recently, our works on high-Q PhC microcavities have achieved great progress.

Here we focus on studying the L3 PhC microcavities formed by removing three cylindrical air holes in the $\Gamma-\mathrm{K}$ direction in a triangular lattice (Fig. 9(a)). The lattice constant is 430 nm, the radius of cylindrical air hole is 120 nm and the thickness of silicon slab is 235 nm. The FDTD calculation results indicate that the L3 PhC microcavities possess a quality factor of about 5300 (Fig. 9(c)). After trying hundreds of simulations, we find that the positions of air holes at the edges of the microcavities affect the Q factor dramatically. The electric field pattern of the cavity mode can be tuned to be Gaussian-type by displacing the six air holes outwardly at the edges of the microcavities, and this can increase the quality factor significantly [42]. The optimal displacement is found to be 73, 10 and 73 nm for the first, second and third air holes at both edges of the microcavities, which is depicted in Fig. 9(b). The maximum quality factor of 127323 (Fig. 9(d)) can be achieved with 20 times larger compared with the unadjusted one.

Based on the optimal parameters, we successfully fabricate the designed high-Q planar L3 PhC microcavities in SOI wafer by implementing EBL and ICP. As can be seen in Fig. 10(a), the L3 microcavity is side-coupled to a W1 waveguide with the barrier of three rows of air holes. The samples are measured by our home-made fiber coupling system as described in the above section. When the incident wavelength is off-resonant, light cannot couple with the microcavity, leading to strong output. While, at resonance most energy is tunneled into the microcavity, resulting in weak output. For the case of high-Q microcavity, a sharp transmission dip is expected in the transmission spectrum. The lattice constant, radius of cylindrical air hole and the thickness of silicon slab are

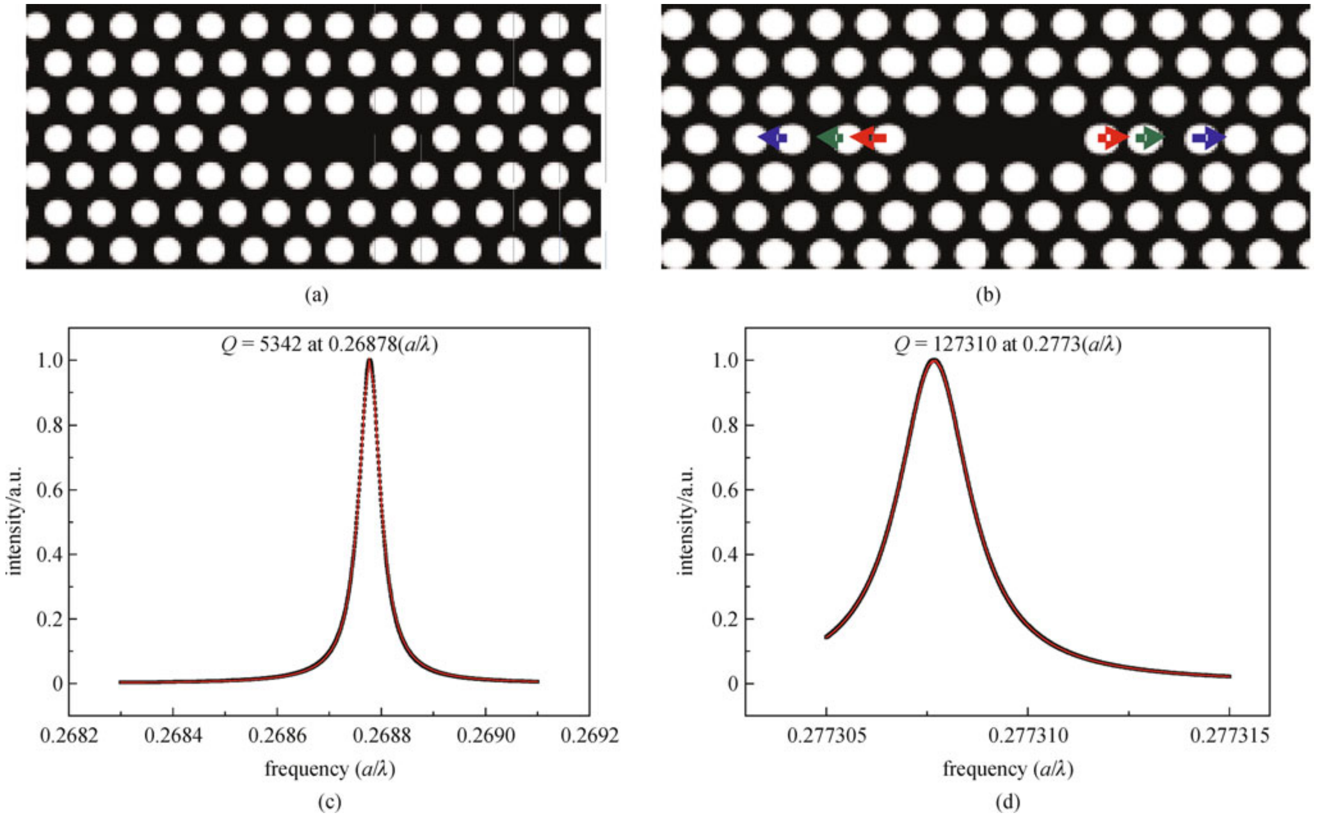

Fig. 9 Schematics of (a) original PhC L3 nanocavity and (b) optimized nanocavity; (c) and (d) show radiation spectra of original PhC L3 nanocavity and optimized nanocavity, respectively

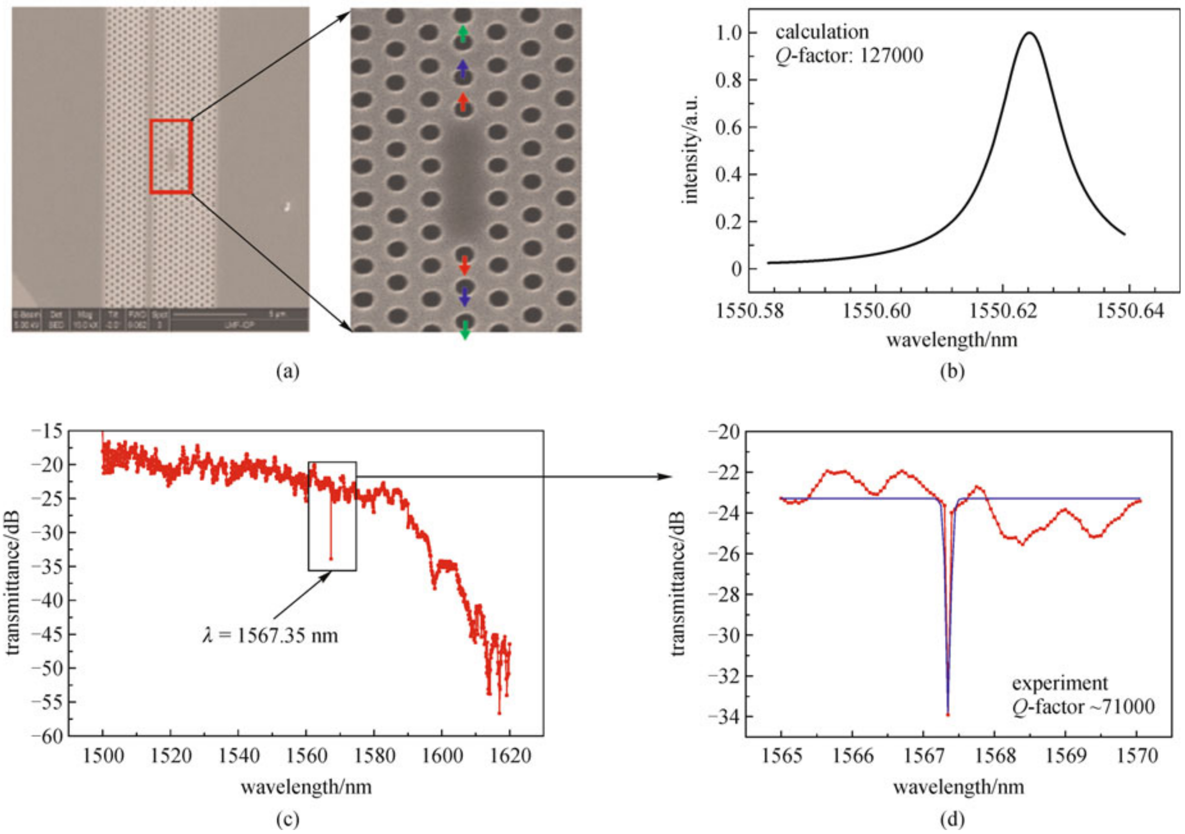

(a) (b)

(c) (d)

Fig. 10 (a) SEM pictures of one of the fabricated samples, including the L3 nanocavtiy with displaced air holes; (b) radiation spectra calculated by FDTD method; (c) and (d) show transmission spectra of one of the fabricated samples. The maximum Q value of up to 71000 is obtained

430, 120 and 235 nm, respectively. Limited by the fabrication accuracy of 10 nm, the displacement is adjusted to be 80, 20 and 80 nm for the six air holes at both edges of the microcavities. Figure 10(a) shows the enlarged view of the cavity region. A sharp and narrow transmission dip is observed at the 1567.35 nm in the measured transmission spectrum (Fig. 10(c)). For the purpose of extracting the quality factor accurately, we finely tune the wavelength between 1565 and 1570 nm. The measurement spectrum is indicated in Fig. 10(d) and the Q-factor as large as 71243 is obtained. Nevertheless, there are some deviation between the simulation and experiment. For example, the resonant wavelength is 16.75 nm red-shifted from the simulated result and the maximum quality factor is less than 127323 (Fig. 10(b)). We believe that the deviation is caused by the imperfection of the cylindrical air holes and the actual radius is not exactly the same as the value in simulation. The success of fabricating high-Q silicon PhC slab microcavities enables us to investigate various interesting quantum phenomena, such as strong coupling between light and quantum system, quantum information processing technique, single photon source, all-solid quantum manipulation and high-Q biochemistry sensing devices.

4.4 Channel drop filters

Channel drop filters are key components for extraction of light trapped in a point-defect cavity to a neighboring waveguide and they sit on the basis of wave-division multiplexers and demultiplexers. They have great applications in a wide variety of fields, such as photonic integrated circuits, telecommunications, and quantum informatics. Based on the simulation and experiment experiences about PhC waveguides, we design and fabricate an ultra compact three ports filter in 2D air-bridged silicon PhC slab by closing the bus waveguide for 100% reflection feedback. Figure 11(a) shows the SEM picture of the three ports filter structure [43]. This filter was fabricated by EBL and ICP techniques. The lattice constant of the PhC and the radius of the air hole are 430 and 145 nm, respectively. Port 3 is the input waveguide channel, while ports 1 and 2 are two output waveguide channels, respectively. They are formed by missing one row of air holes along the $\Gamma - K$ direction of the triangular-lattice PhC, the so called W1 waveguide. C1 and C2 are two point-defect cavities. The distance between the center of the defect cavity and the neighboring waveguide is 3 rows of holes in the y direction. As seen in Fig. 11(a), the C1 cavity consists of three missing air holes, and the two air holes at the cavity edges are shifted outward by 10 nm apart from the regular positions. Similarly, those of the C2 cavity are shifted by 20 nm. The slight shift of air holes is conducive to confine light inside the cavity and leads to a higher quality factor. Meanwhile, the different shifts of the two cavities make the resonant wavelengths slightly different. The experiment results (Figs. 11(b) and 11(c)) show that the resonant wavelengths of C1 and C2 are 1529.5 and 1531 nm, respectively. The wavelength spacing of the two cavities is about 1.5 nm and might be further reduced by continuously changing the size of the cavity. The full widths at half maximum of the peaks are 1.5 and 1.4 nm and the corresponding quality factors are about 1020 and 1090, respectively. To estimate the drop efficiency, a reference straight waveguide of the same parameters is positioned near the three-port filter. By keeping the same intensity of input light, the transmission intensities of the reference waveguide and port 1 are 0.330 and 0.158 μw, respectively, when the input wavelength is set at 1529.5 nm. The drop efficiency of port 1 is roughly estimated to be 48% and a similar result has been obtained at port 2.

It has been well known that structure is the kernel of filter design. Usually, the regulation of microcavity resonant frequency is obtained by changing the size of the cavities. We have proposed a new way to design multi-channel filters by changing the shape of the air holes [44]. When the shape of the air holes changes from circle to ellipse, two parameters, the ellipticity and the orientation angle of the ellipse, in addition to its size can be further explored and they can have a great influence on localized cavity modes. Therefore, we can use this for some special purpose.

Figure 12(a) schematically shows a one-channel PhC filter. A horizontal channel (W1 waveguide) serves as the input signal channel, which is created by removing a single line of air holes along the $\Gamma-\mathrm{K}$ direction. A cavity is formed by removing three air holes along the $\Gamma-\mathrm{K}$ direction that is rotated 60° from the W1 waveguide. It is located four rows away from the major channel and is connected with the major channel through an indirect side coupling. Another single-mode waveguide is formed parallel to the cavity and serves as the output signal channel. Figure 12(b) shows an enlarged picture of the filter in the region around the cavity. One of its axes is oriented counterclockwise by an angle θ to the x axis, namely, the input light propagation direction. The sizes of the axes parallel and perpendicular to this orientation are a and b, respectively. Now we have great structural freedom to tune the optical properties of the new PhC filter by changing the parameters of θ, a and b. To show this point, we design and fabricate a four-channel PhC filter by using different cavity parameters as described in Table 1. The SEM picture of the fabricated four-channel filter is displayed in Fig. 13(a). Four cavities are located on the two sides of the central linear W1 waveguide. They are engineered by leaving several air holes unetched in the $\Gamma-\mathrm{K}$ orientation. The input signal propagates upwards from the bottom input ridge waveguide. Each cavity is coupled with another W1 waveguide that is connected to a ridge waveguide, which serves as the output signal channel.

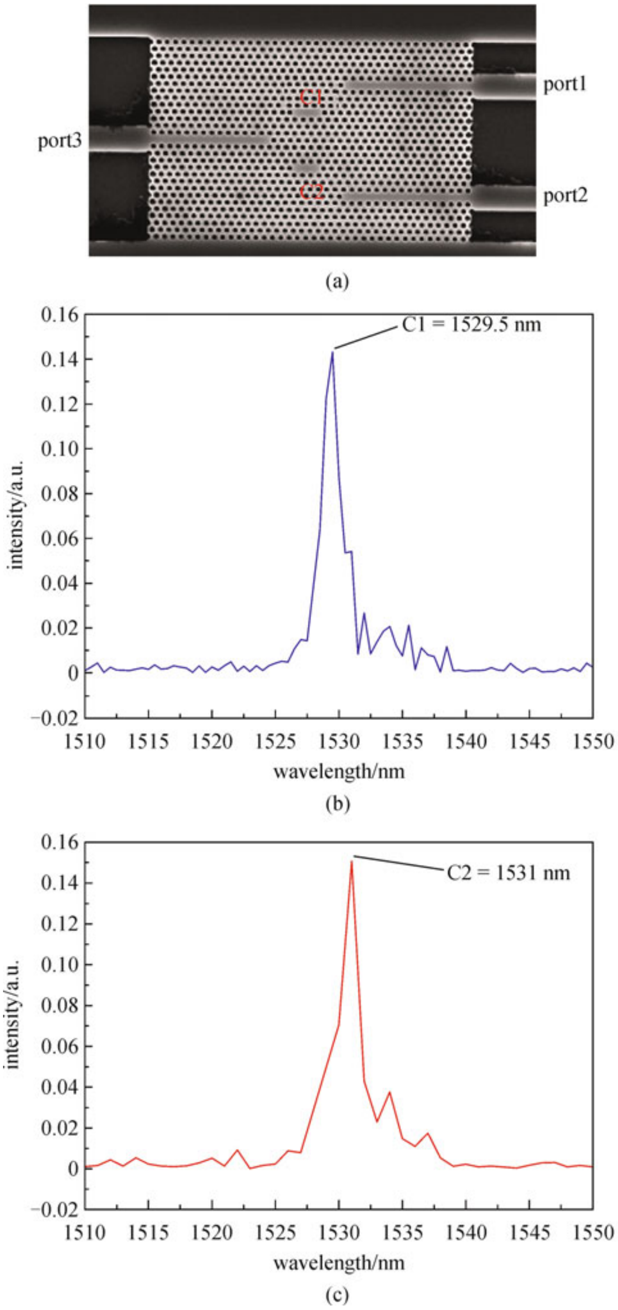

Fig. 11 (a) SEM image of three-port filter; (b) and (c) measured transmission spectra at ports 1 and 2, respectively

Simulation and experimental results of the transmission spectra for the four channels are displayed in Figs. 13(b) and 13(c). Although significant noise exists, a resonant peak can be clearly found for each channel. The peaks are

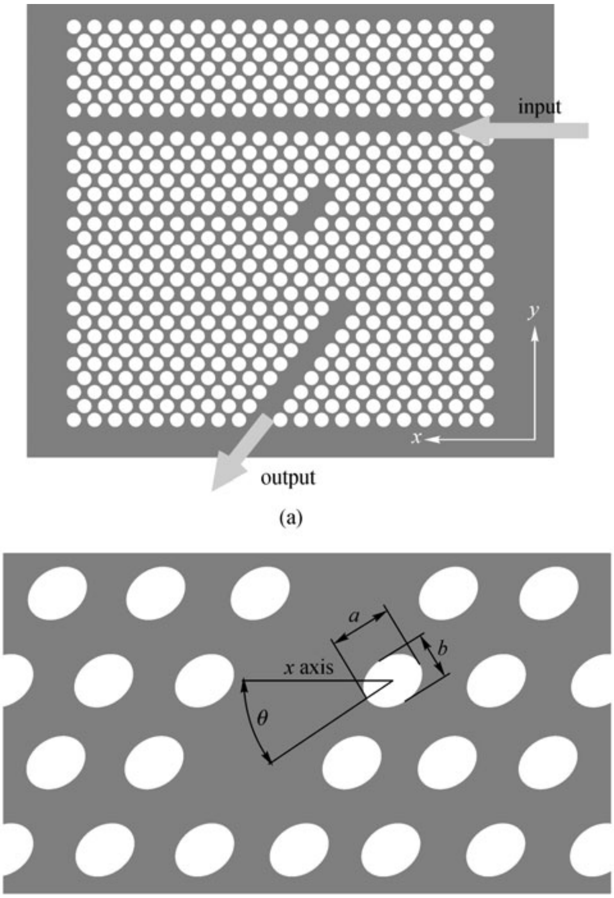

(a)

(b)

Fig. 12 (a) Schematic view of one-channel PhC filter, major channel lies in the *x* direction, and the cavity and output side channel are parallel to Γ–K direction of triangular lattice; (b) enlarged view of the filter around the cavity. Air holes have a general elliptical shape with one of its axes oriented counter-clockwise by an angle *θ* with respect to *x* axis. The two axes are of size *a* and *b*, respectively

located at 1549, 1541, 1567, and 1560 nm for channels 1, 2, 3, and 4, respectively. The results confirm that the air-hole shape has a great influence on the functionality of the PhC filter devices. The elliptical air holes can induce a fine tuning of the resonant wavelength by changing the ellipticity of the elliptical air holes.

As described in the preceding section, a high-performance wide-band Γ−M waveguide can be formed by modifying the radii of the air holes along the pathway. The combination of Γ−M waveguides and Γ−K waveguides can offer a more flexible way to interconnect and couple between different devices. We have proposed a type of PhC filter using these two kinds of waveguides [45]. The Γ−M waveguide and Γ−K waveguide are used as the input and output signal channels respectively, and they are connected via cavity resonance. Figure 14(a) shows the SEM picture of a four-channel filter structure. We change the size of the cavities by moving the end points of the

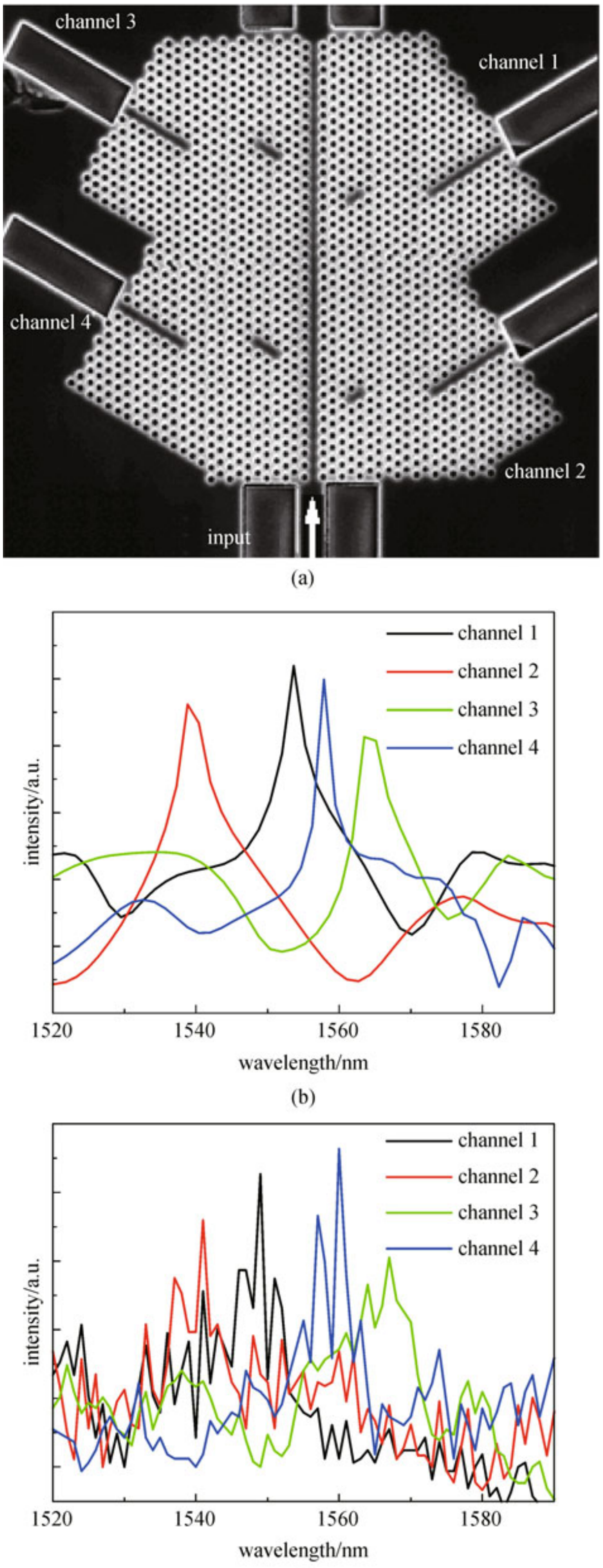

(a)

(b)

(c)

Fig. 13 (a) SEM image of four-channel filter; (b) simulation results of transmission spectra for four-channel filter; (c) experiment results of transmission spectra for the same filter

Table 1 Structural parameters in four-channel filter

channel	lattice constant /nm	number of missing air holes in cavities	long axis a /nm	shot axis b /nm	angle θ	theoretical resonant peak /nm	measured resonant peak /nm	deviation /nm
1	420	2	240	200	0	1553	1549	4
2	430	2	260	240	0	1539	1541	2
3	420	3	240	220	0	1563	1567	4
4	430	3	280	240	0	1558	1560	2

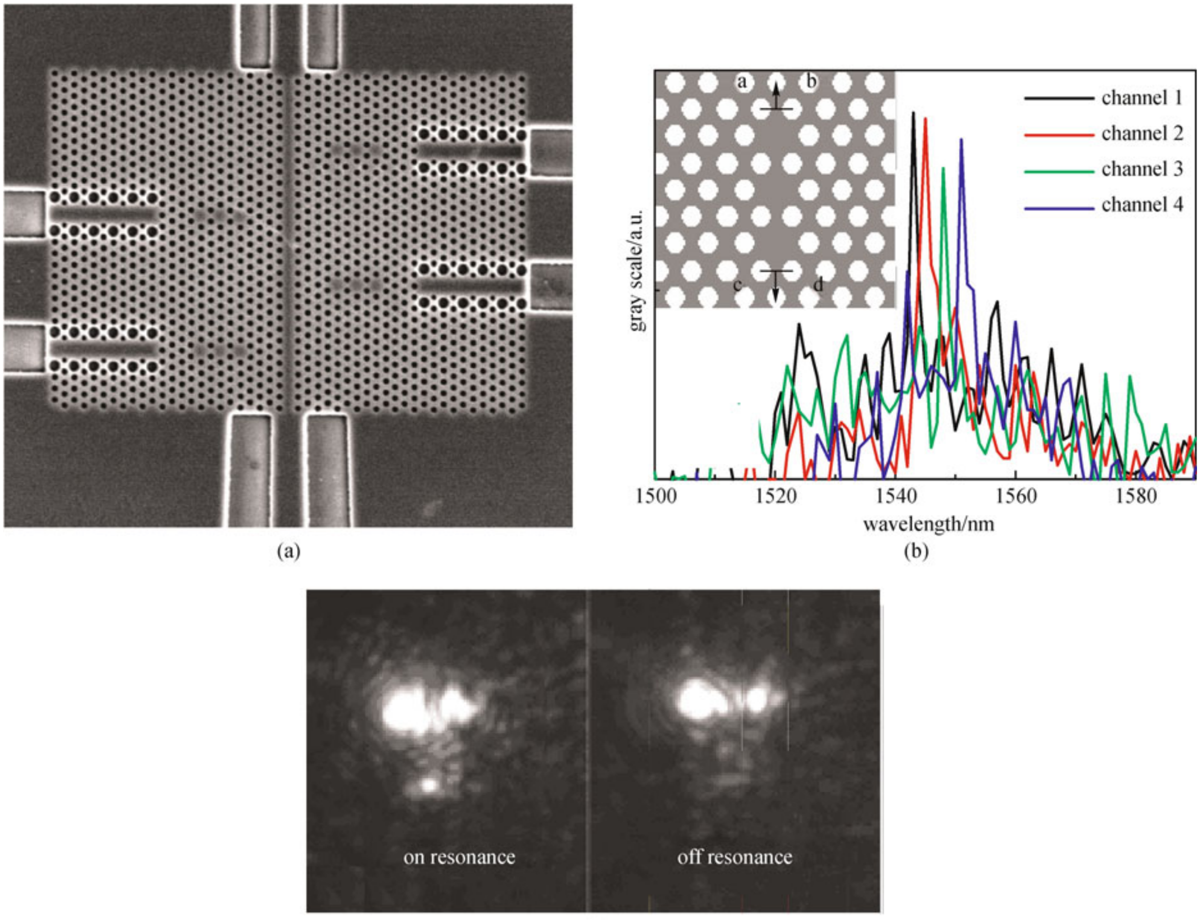

(a) (b)

(c)

Fig. 14 (a) SEM image of fabricated four-channel filter. Four cavities are located on two sides of input waveguide; (b) experimental transmission spectra of the four channel filter in linear scale. Inset: illustrates two groups of end points (air-hole centers) of cavity marked with "a, b" and "c, d." Black arrows: moving direction of these air holes; (c) infrared CCD camera imaging of output signal observed in experiment for one channel of the sample. Bright spot appears at the end of the output channel when the input wavelength coincides with the resonant wavelength and disappears when it is at off-resonance

cavity (marked with "a, b" and "c, d" as shown in the inset of Fig. 14(b)) to change the resonant frequency. Table 2 gives the detailed parameters of the four cavities. The experiment demonstrates that the four resonant peaks are at the wavelengths of 1543, 1545, 1548 and 1551 nm, as shown in Fig. 14(b). In spite of the slight shift in the resonant peak toward higher frequency, which we believe is induced by the uncertainties in the fabrication, the experimental results are in fairly good agreement with the simulation results, where the maximum relative deviation of resonant wavelength is within 2 nm. These results clearly demonstrate that the designed $\Gamma-\mathrm{M}$ waveguides can act together with the usual $\Gamma-\mathrm{K}$ waveguide to construct high-performance multichannel filers with more structural flexibility. In our experiment, we also use the CCD camera to directly monitor the transport of infrared signal within the channel-drop filter. The situation of on-resonance and off-resonance can be clearly visualized and

Table 2 Structural parameters in the four channel $\Gamma-\mathrm{M}$ and $\Gamma-\mathrm{M}$ waveguides filter

channel	end points moving distance/nm	theoretical resonant peak/nm	measured resonant peak/nm	theoretical distance from channel 1/nm	experimental distance from channel 1/nm	deviation /nm
1	0	1550	1543	–	–	–
2	5	1551.5	1545	1.5	2	0.5
3	10	1553	1548	3	5	2
4	15	1556	1551	6	8	2

distinguished from the CCD camera images. One typical case is shown in Fig. 14(c).

5 PhC band-engineering devices for anomalous transport control

In previous sections, we discuss several PhC devices, including waveguides, cavities, and channel-drop filters that are built on the silicon 2D PhC platform. These devices work on defects that are brought into PBG and they can be considered as PBG materials. As we have mentioned, PhC structures possess another important feature: photonic pass bands. Here we show an example device that implements the dispersion and refraction properties of PhCs at their transmission bands. Figure 15(a) shows the typical photonic bands structure of an air-bridge PhC slab structure composed of a square-lattice array of air holes etching in silicon slab. The areas labeled in Fig. 15(a) show the unconventional light propagation, self-collimation and negative refraction, in PhC. One effective way to understand and exploit desirable light propagation properties in PhC is using the equifrequency surface (EFS) contours, as shown in Figs. 13(b) and 13(c). Figure 15(b) shows the EFS contours of the first TE-like band. The EFS contours in the red line frame are flat, meaning that this is the self-collimation region. If light propagates along the $\Gamma-\mathrm{M}$ direction, it does not suffer any diffraction in the PhC. $\Gamma=(0,0)(\pi/a)$ and $\mathrm{M}=(1,1)\times(\pi/a)$ are high-symmetric points in the first Brillouin zone for square lattice. This kind of PhC structures can be used as the channelless waveguide in integrated optic devices. Figure 15(c) shows EFS contours of the second band. The EFS contours are roughly circular around the direction at the reduced frequency (a/λ) range 0.28–0.31, as indicated in the red solid line frame. When the frequency increases, the EFS contours move toward the Γ point, which indicates the existence of negative refraction in the region. If the incident light is mainly parallel to the $\Gamma-\mathrm{M}$ direction, the PhC will behave like an isotropic medium with a negative index of refraction in that particular frequency range.

5.1 Negative refraction

Basing on the above analysis, we designed and fabricated an air-bridged PhC structure that exhibited negative refraction of infrared light [46]. The structure is schematically shown in Fig. 16(a). These structures are directly drilled by FIB technique. The input infrared signal channel is a silicon wire waveguide, which is inclined with respect to the surface normal by 10°. The lattice constant a of the square array is 460 nm and the diameter of the air hole is 220 nm. We first use 3D FDTD method to simulate the EM field intensity distribution at wavelength 1503 nm. The result is displayed in Fig. 16(b). We find strong reflection and scattering at the interface between the input waveguide and the PhC structure. This is induced by the serious impedance mismatch at the interface, although the high index contrast air-bridged structure can achieve good optical confinement. To surpass this obstacle, we use a tapered air-holes connection layer at the input surface of PhC structure to reduce the reflection and scattering losses. As shown in Fig. 16(b), a large fraction of light power from the input waveguide is coupled into the PhC structure and negative refraction of light beam within the PhC structure is clearly seen. Besides, the reflection or scattering of light at the input interface of the PhC is very much reduced. This clearly indicates that the designed tapered interface can reduce the interface impedance mismatch remarkably. The calculated value of negative refraction angle is $-45°$.

In our measurement, TE-polarized light from a tunable semiconductor laser (1500–1640 nm) was first launched into a tapered single mode fiber, and then coupled to the silicon wire waveguide, and finally incident on the PhC structure. The ordinary way to see the light propagation behavior is to directly observe the pattern of the radiated light from the top of the sample using a conventional microscopy objective and an infrared CCD camera. The result is shown in Fig. 16(c). The light spot at the middle bottom part of the pattern is the radiated light from the input silicon wire waveguide. The big light spot at the center represents the scattered light at the interface between the input wire waveguide and the PhC due to impedance mismatch. There is also a small bright spot at the top right corner of the pattern, and it is recognized to result from the radiated light when the negative refraction beam hits the end facet of the PhC structure. Because the TE-like modes are strongly confined guided mode on the silicon slab and the surface fields are nonradiative and evanescent with respect to the vertical direction of the PhC slab, the far-field pattern observed and recorded by the ordinary optical microscopy is not able to reveal the detailed process about how the negative refraction beam propagates inside the PhC structure unless the scattering of light by roughness and irregularity is sufficiently strong on the beam propagation path. This is indeed the case for Fig. 16(c). In fact, the small bright spot could not appear without the intentional introduction of the air slot at the far end of the PhC structure. It would not be possible to tell which way the infrared beam would refract if without the aid of this scattering light spot.

In order to observe clearly and tell unambiguously the ray trace of the negative refraction beam in the PhC structure, we used the SNOM technology (SNOM-100 Nanonics, Israel). A probe scans in the vicinity of the surface of the PhC structure and records the near-field intensity distribution. The tip has a resolution of about 100 nm, i.e., 1/15 of the wavelength. The signal is recorded by an infrared single-photon detector, which allows us to capture very weak infrared signals. The probed near field information directly reflects light propagation properties of the TE-like modes for the PhC and enables one to visualize the ray trace of the negative refraction light beam because the near field at the surface is an integral part of the modal profile of the confined guided modes that exponentially decay away from the surface of the slab. In the SNOM picture (Fig. 16(d)), a bright spot also appears at the front interface of the PhC structure, but it is much smaller than the one in Fig. 16(c). The ray trace of the incident light beam along the silicon wire waveguide and its propagation along the negative refraction direction inside the PhC structure can be clearly seen. The negative refraction angle is about −45°, which is in good agreement with the FDTD simulation presented in Fig. 16(b). The SNOM detection unambiguously discloses the negative refraction property of the designed PhC.

On the other hand, ordinary positive refraction only occurs for TM-like confined modes, so the designed PhC structure can behave as an efficient beam splitter in an integrated optical circuit. The high-resolution SNOM technology can greatly help one to directly visualize the ray trace and acquire deeper understanding on various anomalous wave propagation behaviors, such as super-prism, superlensing, self-collimation, and slow light in deliberately designed 2D PhC slab structures in the optical wavelengths. This in turn can help to explore a wider regime of controlling light behaviors on the nanoscale for future basic science and high technology applications.

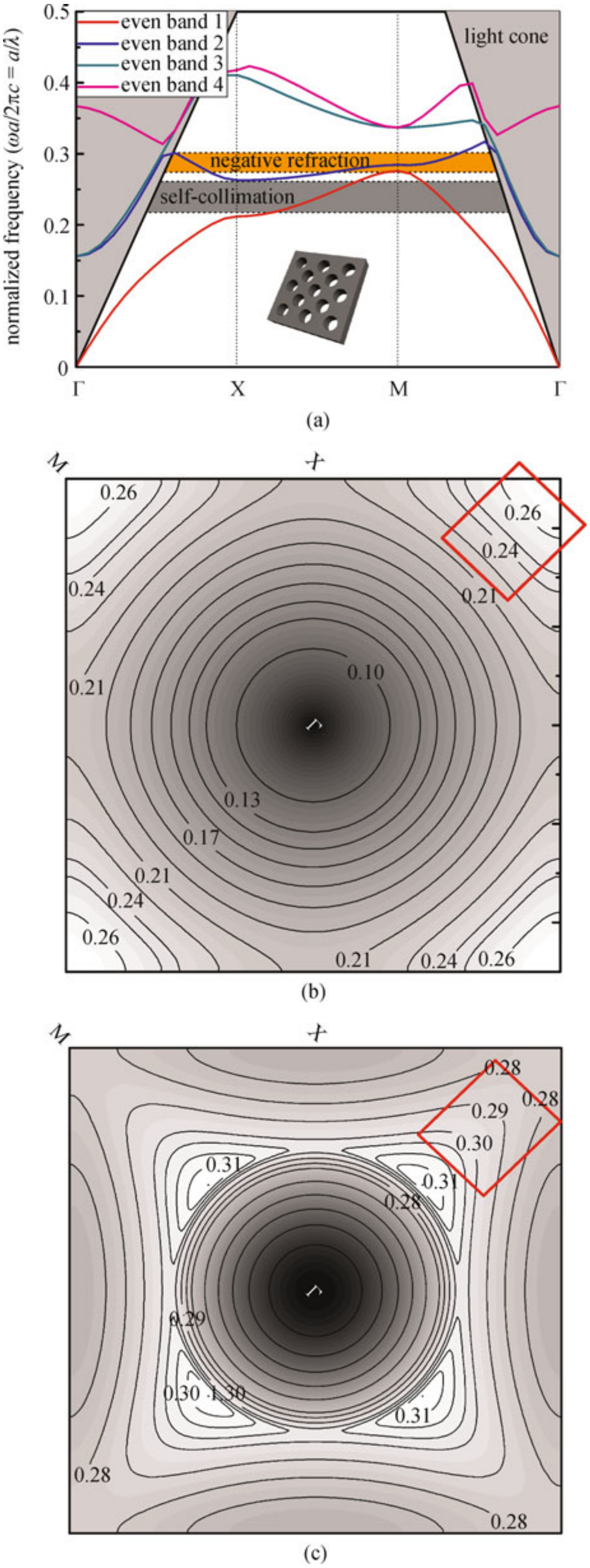

(a)

(b)

(c)

Fig. 15 (a) (Color online) Photonic band structures of TE-like bands for air-holes square-lattice PhC slab; (b) EFS contours of TE-like first band for the same PhC show that self-collimation can occur in the direction around the Γ–M direction; (c) EFS contours of the TE-like second band show that negative refraction can occur in the direction around the Γ–M direction

5.2 Self-collimation effect

Self-collimation effect is the propagation of light without diffraction along the propagation direction. This phenomenon has been used to non-channel waveguides, beam splitters and beam combiners [47–49]. Therefore, the behaviors of these devices are determined by the

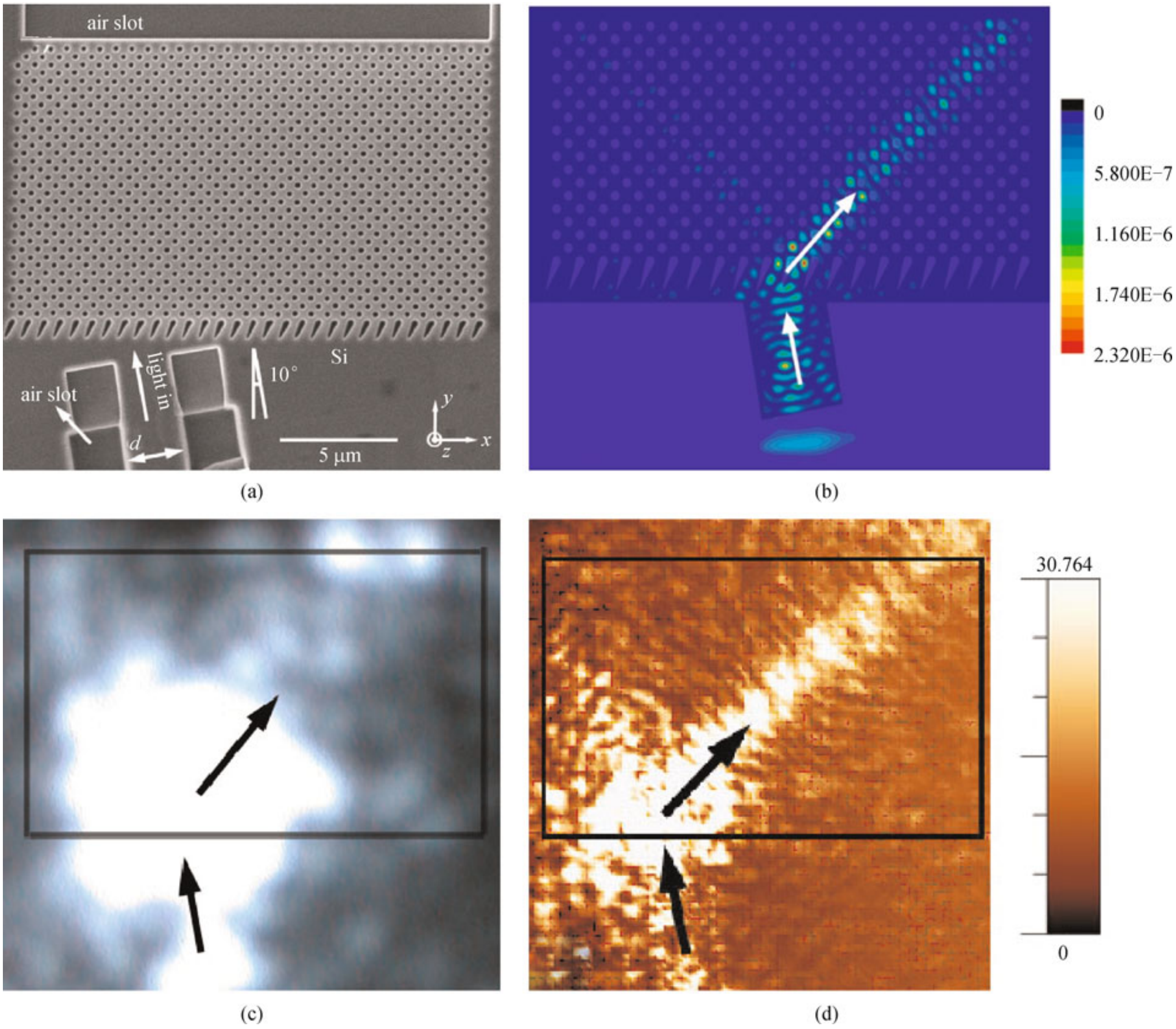

(a) (b) (c) (d)

Fig. 16 (a) SEM picture of PhC structure and input waveguide. The width of the waveguide d is 2 μm; (b) light intensity distribution of TE-like modes for PhC with deliberately designed tapered air-holes interface; (c) directly observed pattern of radiated light of $\lambda = 1500$ nm from the top using an objective lens; (d) SNOM picture of the negative refraction of the same wavelength. In each picture, the boundary of the PhC structure is superimposed as solid lines

performance of the self-collimation effect. Here, we analyze a simple structure composed by a square lattice array of elliptical air-holes. Broadband large-angle self-collimation effect is observed for TE-like guided modes in infrared wavelength in our structure.

Figure 17(a) shows our PhC structure formed by a square lattice of elliptical holes. The calculated TE mode photonic band diagram of the fourth, fifth and sixth bands are shown in Fig. 17(b). The self-collimation effect can be observed at the gray regions within a broad normalized frequency range $0.36-0.39$ and $0.43-0.46$. For simplicity, we only consider the EFS contours of the fifth TE band (Fig. 17(c)). The contours are flat at the normalized frequency between 0.43 and 0.46 for all the values of k_y and not just in the vicinity of $k_y = 0$. This feature indicates that our structure can support self-collimation for incident light beams with large incident angles. Then the FDTD simulation by using the MEEP package is performed to verify our prediction. A structure with the size of $30a \times 45a$ is considered here. A Gaussian beam with a width of $4a$ propagates into the surface at 0°, 20° and 60° incident angles (Fig. 18). For simplicity, here we only consider the minimum (0.36) and the maximum normalized frequency (0.43). Figure 18 shows the electric field intensity distribution in the xy plane with 0°, 20° and 60° incident angles at normalized frequency 0.36 (Fig. 18(a)) and 0.46 (Fig. 18(b)). From the simulation results, we find that the light beam is collimated along the propagation direction for each situation. However, the couple efficiency of the incident light becomes lower and lower with the increase of the incident angle. We do not show the field distributions for those incident angles that are larger than

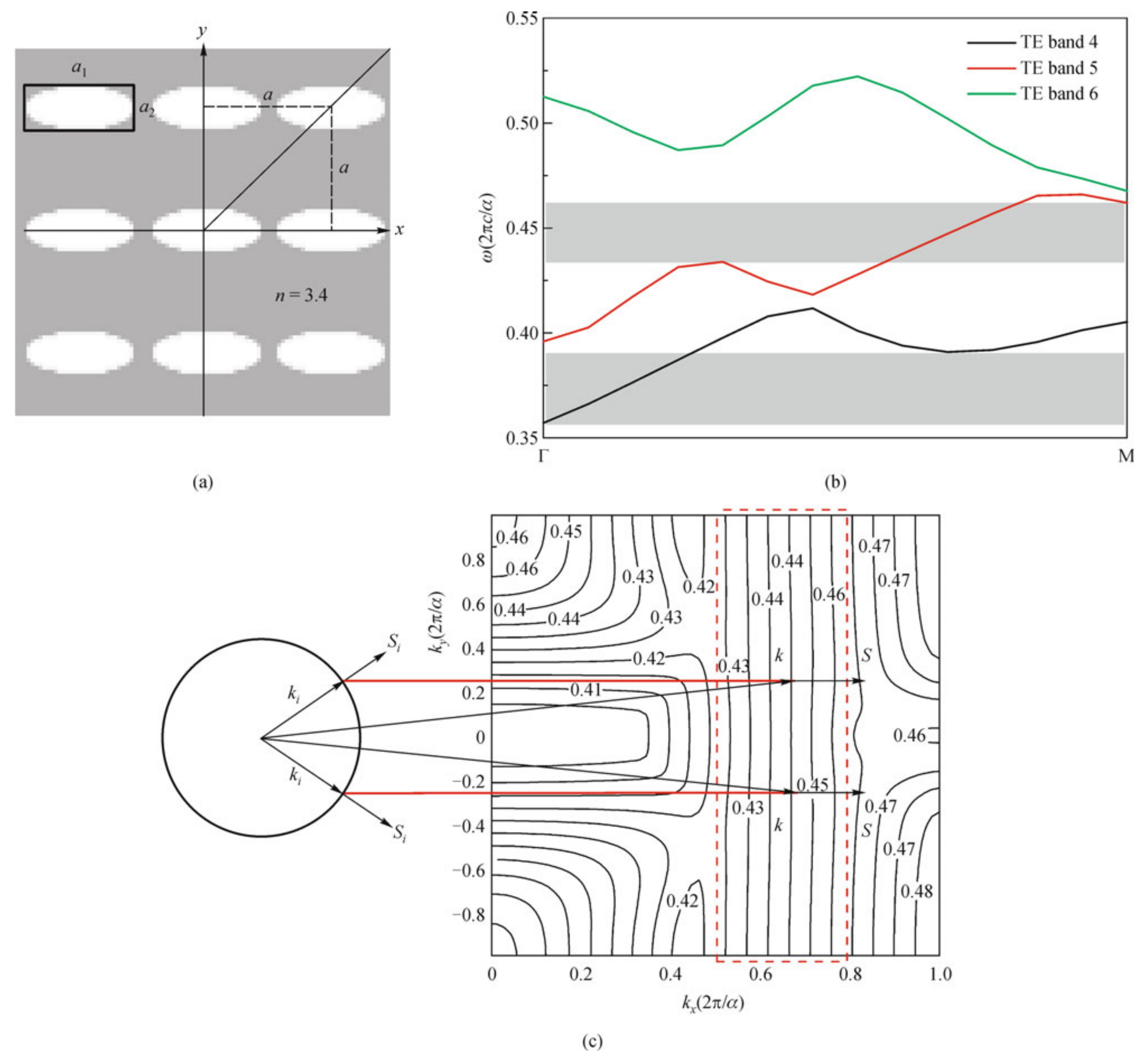

(a) (b) (c)

Fig. 17 (a) Schematic of PhC structure formed by square lattice of elliptical holes; (b) band diagram of the fourth, fifth and sixth TE bands; (c) EFS contours of the fifth TE band

60°. These six situations in Fig. 18 are sufficient to show the broadband large-angle characteristic of the self-collimation effect.

Following our simulation results, we fabricate our PhC structures in SOI substrate by EBL and ICP etching process. Figure 19 shows the SEM pictures of the designed PhC structures with 0°, 20° or 60° incident waveguides. Ray trace of light beam is observed using IR camera and a high numerical aperture (NA = 0.50) objective. Detailed images of the field intensity of the scattered light are recorded for 0°, 20° and 60° incident angles for different incident wavelengths. Here we only show the patterns of the minimum and maximum wavelengths for each incident angle. They demonstrate strong light confinement along the propagation direction for all the situations. The experimental results are in good agreement with FDTD simulations. We believe that this kind of structure may have potential applications in beam combiners and multiplexers.

6 Conclusions

We have presented recent progresses on infrared 2D air-bridged silicon PhC slab devices that were made in our group in the past several years. 2D air-bridged silicon PhC slab structures can confine light by the high index contrast in the vertical off-plane direction and manipulate light by

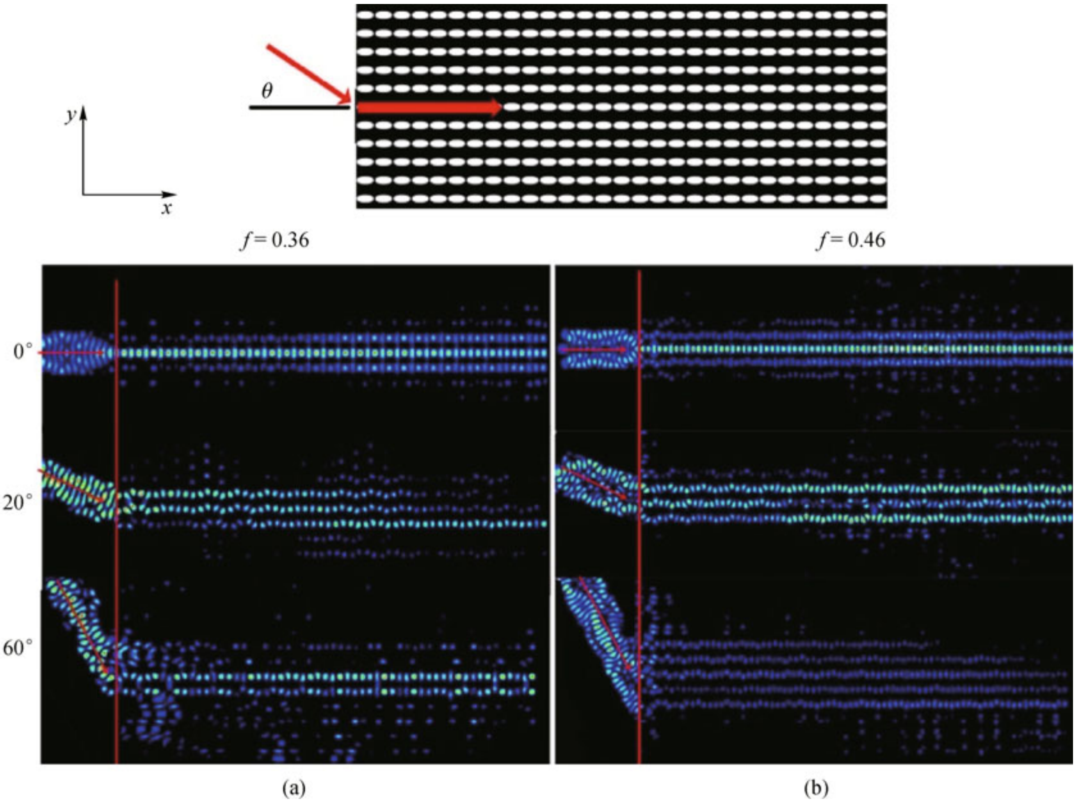

Fig. 18 Electric field intensity distribution with 0°, 20° and 60° incident angles at the minimum normalized frequency 0.36 (a) and the maximum 0.46 (b). A FDTD method is used in the simulations

photonic band and band gaps in the lateral in-plane direction. In addition, silicon is transparent and has a large refractive index in the infrared wavelengths. Therefore, the air-bridged silicon PhC structures become one of the most important elements in integrated optics.

In this review, we have discussed several integrated optical elements and devices in regard to their design, fabrication, and characterization. These devices are based on either the PBG or photonic band structure engineering. To bring these devices into reality, we have made extensive efforts to construct high-efficiency numerical simulation tools for solution of photonic band structures, transmission spectra, light propagation dynamics, light wave patterns, and many others. These simulations allow for design of optimized PhC structures for a specific application. The fabrication of these devices strongly depends on state-of-the-art nanofabrication technologies including EBL, FIB, ICP etching, and other wet etching techniques and procedures. We have constructed a convenient experimental setup to measure the transmission spectra and monitor the propagation path of infrared signals within PhC structures simultaneously. The setup makes the optical characterization of PhC devices accurate, user-friendly, fast, and convenient.

We have proposed $\Gamma-\mathrm{M}$ waveguides made in 2D triangular-lattice PhC slabs. After a series of optimization and improvement, we find out the optimized geometries for high performance wide band $\Gamma-\mathrm{M}$ waveguides. As the $\Gamma-\mathrm{M}$ waveguide is perpendicular to the usual $\Gamma-\mathrm{K}$ waveguide, we combine the $\Gamma-\mathrm{K}$ waveguide and $\Gamma-\mathrm{M}$ waveguide together to form 90° waveguide bends and channel drop filters. The combination of $\Gamma-\mathrm{M}$ waveguide and $\Gamma-\mathrm{K}$ waveguide can offer a flexible way to interconnect and couple between different devices. In addition, we have shown design of two other kinds of channel drop filters. They achieve fine tuning of the resonant wavelengths by changing the size of the cavities or the shape of the air holes around the cavities. We have also designed and realized PhC waveguide based on the coupled-cavity scheme. There are a lot of geometric parameters to fine tune the light transport properties in the structure. Moreover, we have successfully fabricated high-*Q* silicon PhC microcavities with a *Q*-factor up to 70000 and this paves the way to experimentally explore light-matter interaction within the strong-coupling regime in the all-solid platform.

We have also investigated optical devices that work on band structure engineering. We have explored PhC structures that exhibit interesting and useful dispersion and refraction properties, such as negative refraction and self-collimation effects. We have designed and fabricated a kind of PhC structure with negative refraction effect and

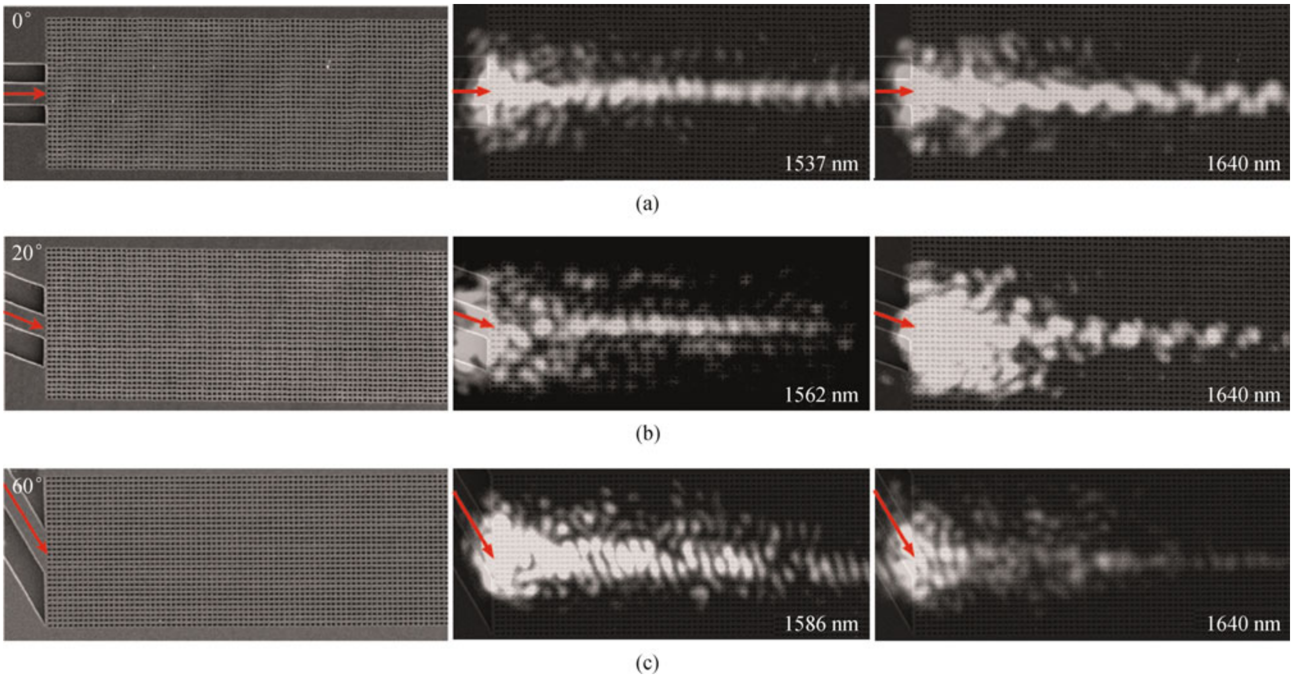

Fig. 19 Left panels: SEM pictures of designed PhC structures with 0° (a); 20° (b) and 60° (c) incident waveguide. Middle and right panels: Ray trace of light beam observed using IR camera and a high numerical aperture (NA = 0.50) objective. The patterns of the minimum and maximum wavelengths are shown for each incident angle

use SNOM technology to observe the negative refraction ray trace of infrared light beam. In addition, we obtain broadband large-angle self-collimation effect for TE-like guided modes in infrared wavelength. All of these results show that 2D air-bridged silicon PhC structures can control light propagation in many flexible ways and have many potential applications in all-optical integrated circuits and other fields. The efforts that we have made and the experiences that we have accumulated in the past several years will allow us to design and realize PhC devices with novel functionalities.

Acknowledgements This work was supported by the National Key Basic Research Special Foundation of China (No. 2011CB922002), the National Natural Science Foundation of China, and National Center for Nanoscience and Technology of China. The authors would like to thank the previous members of our group, Cheng Ren, Haihua Tao, Yazhao Liu, and Changzhu Zhou for their contributions to the works presented in this review.

References

1. Yablonovitch E. Inhibited spontaneous emission in solid-state physics and electronics. Physical Review Letters, 1987, 58(20): 2059–2062
2. Joannopoulos J D, Johnson S G, Winn J N, Meade R D. Photonic Crystals: Molding the Flow of Light. 2nd ed. Princeton: Princeton University Press, 2008
3. Valentine J, Zhang S, Zentgraf T, Ulin-Avila E, Genov D A, Bartal G, Zhang X. Three-dimensional optical metamaterial with a negative refractive index. Nature, 2008, 455(7211): 376–379
4. Yao J, Liu Z W, Liu Y M, Wang Y, Sun C, Bartal G, Stacy A M, Zhang X. Optical negative refraction in bulk metamaterials of nanowires. Science, 2008, 321(5891): 930
5. Johnson S G, Fan S H, Villeneuve P R, Joannopoulos J D, Kolodziejski L A. Guided modes in photonic crystal slabs. Physical Review B: Condensed Matter and Materials Physics, 1999, 60(8): 5751–5758
6. Painter O, Lee R K, Scherer A, Yariv A, O'Brien J D, Dapkus P D, Kim I. Two-dimensional photonic band-gap defect mode laser. Science, 1999, 284(5421): 1819–1821
7. McNab S J, Moll N, Vlasov Y A. Ultra-low loss photonic integrated circuit with membrane-type photonic crystal waveguides. Optics Express, 2003, 11(22): 2927–2939
8. Luo C Y, Johnson S G, Joannopoulos J D, Pendry J B. All-angle negative refraction without negative effective index. Physical Review B: Condensed Matter and Materials Physics, 2002, 65 (20): 201104
9. Kosaka H, Kawashima T, Tomita A, Notomi M, Tamamura T, Sato T, Kawakami S. Self-collimating phenomena in photonic crystals. Applied Physics Letters, 1999, 74(9): 1212–1214
10. Yu X F, Fan S H. Bends and splitters for self-collimated beams in photonic crystals. Applied Physics Letters, 2003, 83(16): 3251–3253
11. Kosaka H, Kawashima T, Tomita A, Notomi M, Tamamura T, Sato T, Kawakami S. Superprism phenomena in photonic crystals: toward microscale lightwave circuits. Journal of Lightwave Technology, 1999, 17(11): 2032–2038
12. Baba T, Matsumoto T, Echizen M. Finite difference time domain

study of high efficiency photonic crystal superprisms. Optics Express, 2004, 12(19): 4608–4613

13. Berrier A, Mulot M, Swillo M, Qiu M, Thylén L, Talneau A, Anand S. Negative refraction at infrared wavelengths in a two-dimensional photonic crystal. Physical Review Letters, 2004, 93(7): 073902
14. Born M, Wolf E, Bhatia A B. Principles of Optics: Electromagnetic Theory of Propagation, Interference and Diffraction of Light. New York: Cambridge University Press, 1999
15. Ho K M, Chan C T, Soukoulis C M. Existence of a photonic gap in periodic dielectric structures. Physical Review Letters, 1990, 65 (25): 3152–3155
16. Johnson S, Joannopoulos J. Block-iterative frequency-domain methods for Maxwell's equations in a planewave basis. Optics Express, 2001, 8(3): 173–190
17. Li Z Y, Gu B Y, Yang G Z. Large absolute band gap in 2D anisotropic photonic crystals. Physical Review Letters, 1998, 81 (12): 2574–2577
18. Li Z Y, Wang J, Gu B Y. Creation of partial band gaps in anisotropic photonic-band-gap structures. Physical Review B: Condensed Matter and Materials Physics, 1998, 58(7): 3721–3729
19. Pendry J B. Photonic Band Structures. Journal of Modern Optics, 1994, 41(2): 209–229
20. Chan C T, Yu Q L, Ho K M. Order-N spectral method for electromagnetic waves. Physical Review B: Condensed Matter and Materials Physics, 1995, 51(23): 16635–16642
21. Taflove A. Computational Electrodynamics: the Finite-Difference Time-Domain Method. Boston: Artech House, 1995
22. Nicorovici N A, McPhedran R C, Botten L C. Photonic band gaps for arrays of perfectly conducting cylinders. Physical Review E: Statistical Physics, Plasmas, Fluids, and Related Interdisciplinary Topics, 1995, 52(1): 1135–1145
23. Li L M, Zhang Z Q. Muitiple-scattering approach to finite-sized photonic band-gap materials. Physical Review B: Condensed Matter and Materials Physics, 1998, 58(15): 9587–9590
24. Li Z Y, Lin L L. Photonic band structures solved by a plane-wave-based transfer-matrix method. Physical Review E: Statistical, Nonlinear, and Soft Matter Physics, 2003, 67(4): 046607
25. Li Z Y, Lin L L. Evaluation of lensing in photonic crystal slabs exhibiting negative refraction. Physical Review B: Condensed Matter and Materials Physics, 2003, 68(24): 245110
26. Lin L L, Li Z Y, Ho K M. Lattice symmetry applied in transfer-matrix methods for photonic crystals. Journal of Applied Physics, 2003, 94(2): 811–821
27. Li Z Y, Ho K M. Light propagation in semi-infinite photonic crystals and related waveguide structures. Physical Review B: Condensed Matter and Materials Physics, 2003, 68(15): 155101
28. Li Z Y, Lin L L, Ho K M. Light coupling with multimode photonic crystal waveguides. Applied Physics Letters, 2004, 84(23): 4699–4701
29. Che M, Li Z Y. Analysis of photonic crystal waveguide bends by a plane-wave transfer-matrix method. Physical Review B: Condensed Matter and Materials Physics, 2008, 77(12): 125138
30. Che M, Li Z Y. Analysis of surface modes in photonic crystals by a plane-wave transfer-matrix method. Journal of the Optical Society of America a-Optics Image Science and Vision, 2008, 25(9): 2177–2184
31. Li Z Y, Ho K M. Analytic modal solution to light propagation through layer-by-layer metallic photonic crystals. Physical Review B: Condensed Matter and Materials Physics, 2003, 67(16): 165104
32. Li J J, Li Z Y, Zhang D Z. Second harmonic generation in one-dimensional nonlinear photonic crystals solved by the transfer matrix method. Physical Review E: Statistical, Nonlinear, and Soft Matter Physics, 2007, 75(5): 056606
33. Li Z Y, Li J J, Zhang D Z. Nonlinear frequency conversion in two-dimensional nonlinear photonic crystals solved by a plane-wave-based transfer-matrix method. Physical Review B: Condensed Matter and Materials Physics, 2008, 77(19): 195127
34. Oskooi A F, Roundy D, Ibanescu M, Bermel P, Joannopoulos J D, Johnson S G. MEEP: A flexible free-software package for electromagnetic simulations by the FDTD method. Computer Physics Communications, 2010, 181(3): 687–702
35. Shinya A, Mitsugi S, Kuramochi E, Notomi M. Ultrasmall multi-channel resonant-tunneling filter using mode gap of width-tuned photonic-crystal waveguide. Optics Express, 2005, 13(11): 4202–4209
36. Song B S, Nagashima T, Asano T, Noda S. Resonant-wavelength tuning of a nanocavity by subnanometer control of a two-dimensional silicon-based photonic crystal slab structure. Applied Optics, 2009, 48(26): 4899–4903
37. Liu Y Z, Liu R J, Zhou C Z, Zhang D Z, Li Z Y. Gamma-Mu waveguides in two-dimensional triangular-lattice photonic crystal slabs. Optics Express, 2008, 16(26): 21483–21491
38. Zhou C Z, Liu Y Z, Li Z Y. Waveguide bend of 90° in two-dimensional triangular lattice silicon photonic crystal slabs. Chinese Physics Letters, 2010, 27(8): 084203
39. Tao H H, Ren C, Liu Y Z, Wang Q K, Zhang D Z, Li Z Y. Near-field observation of anomalous optical propagation in photonic crystal coupled-cavity waveguides. Optics Express, 2010, 18(23): 23994–24002
40. Hennessy K, Badolato A, Winger M, Gerace D, Atatüre M, Gulde S, Fält S, Hu E L, Imamoğlu A. Quantum nature of a strongly coupled single quantum dot-cavity system. Nature, 2007, 445(7130): 896–899
41. Yoshie T, Scherer A, Hendrickson J, Khitrova G, Gibbs H M, Rupper G, Ell C, Shchekin O B, Deppe D G. Vacuum Rabi splitting with a single quantum dot in a photonic crystal nanocavity. Nature, 2004, 432(7014): 200–203
42. Akahane Y, Asano T, Song B S, Noda S. High-*Q* photonic nanocavity in a two-dimensional photonic crystal. Nature, 2003, 425 (6961): 944–947
43. Ren C, Tian J, Feng S, Tao H H, Liu Y Z, Ren K, Li Z Y, Cheng B Y, Zhang D Z, Yang H F. High resolution three-port filter in two dimensional photonic crystal slabs. Optics Express, 2006, 14(21): 10014–10020
44. Liu Y Z, Feng S A, Tian J, Ren C, Tao H H, Li Z Y, Cheng B Y, Zhang D Z, Luo Q. Multichannel filters with shape designing in two-dimensional photonic crystal slabs. Journal of Applied Physics, 2007, 102(4): 043102
45. Liu Y Z, Liu R J, Feng S A, Ren C, Yang H F, Zhang D Z, Li Z Y. Multichannel filters via Γ-M and Γ-K waveguide coupling in two-dimensional triangular-lattice photonic crystal slabs. Applied

Physics Letters, 2008, 93(24): 241107

46. Gan L, Liu Y Z, Li J Y, Zhang Z B, Zhang D Z, Li Z Y. Ray trace visualization of negative refraction of light in two-dimensional air-bridged silicon photonic crystal slabs at 1.55 μm. Optics Express, 2009, 17(12): 9962–9970
47. Nguyen H M, Dundar M A, van der Heijden R W, van der Drift E W J M, Salemink H W M, Rogge S, Caro J. Compact Mach-Zehnder interferometer based on self-collimation of light in a silicon photonic crystal. Optics Express, 2010, 18(7): 6437–6446
48. White T P, de Sterke C M, McPhedran R C, Botten L C. Highly efficient wide-angle transmission into uniform rod-type photonic crystals. Applied Physics Letters, 2005, 87(11): 111107
49. Zengerle R. Light-propagation in singly and doubly periodic planar wave-guides. Journal of Modern Optics, 1987, 34(12): 1589–1617